Journal of Geophysical Research: Space Physics

RESEARCH ARTICLE
10.1029/2018JA025664

Roles of Flow Braking, Plasmaspheric Virtual Resonances, and Ionospheric Currents in Producing Ground Pi2 Pulsations

Kazue Takahashi[1], Michael D. Hartinger[2], Massimo Vellante[3,4], Balázs Heilig[5], Robert L. Lysak[6], Dong-Hun Lee[7], and Charles W. Smith[8]

[1]The Johns Hopkins University Applied Physics Laboratory, Laurel, MD, USA, [2]Bradley Department of Electrical and Computer Engineering, Virginia Polytechnic Institute and State University, Blacksburg, VA, USA, [3]Department of Physical and Chemical Sciences, University of L'Aquila, L'Aquila, Italy, [4]Consorzio Area di Ricerca in Astrogeofisica, L'Aquila, Italy, [5]Mining and Geological Survey of Hungary, Budapest, Hungary, [6]School of Physics and Astronomy, University of Minnesota, Minneapolis, MN, USA, [7]Department of Astronomy and Space Science, Kyung Hee University, Yongin, South Korea, [8]Department of Physics and Institute for the Study of Earth, Oceans, and Space, University of New Hampshire, Durham, NH, USA

Key Points:
- Periodic oscillation of earthward plasma flow triggered a Pi2 pulsation event observed in the plasmasphere and on the ground
- In the plasmasphere, the event was detected as multifrequency poloidal oscillations consistent with virtual resonances
- Low-latitude ground magnetometers detected the plasmaspheric spectral components both on the nightside and dayside

Correspondence to:
K. Takahashi,
kazue.takahashi@jhuapl.edu

Citation:
Takahashi, K., Hartinger, M. D., Vellante, M., Heilig, B., Lysak, R. L., Lee, D.-H., & Smith, C. W. (2018). Roles of flow braking, plasmaspheric virtual resonances, and ionospheric currents in producing ground Pi2 pulsations. *Journal of Geophysical Research: Space Physics*, *123*. https://doi.org/10.1029/2018JA025664

Received 9 MAY 2018
Accepted 25 SEP 2018
Accepted article online 28 SEP 2018

Abstract In one model, Pi2 pulsations are driven pulse by pulse by fast mode pulses that are launched as periodic bursty bulk flows brake when they approach the Earth. We have examined this model by analyzing data from multiple spacecraft and ground magnetometers for a Pi2 pulsation event. During the event, which started at ~2226 UT on 8 November 2014, Time History of Events and Macroscale Interactions during Substorms (THEMIS)-D detected an ~2-min-period plasma bulk flow oscillation in the near-Earth magnetotail, while THEMIS-E and Van Allen Probes-B, both located on the nightside just earthward of the electron plasmapause, detected a Pi2 pulsation consisting of a 10-mHz oscillation in the azimuthal component of the electric field and a 19-mHz oscillation in the compressional component of the magnetic field. On the ground, magnetic field oscillations containing both frequencies were observed both on the nightside and on the dayside. The nightside observations indicated that the pulsation had a radially standing structure, which is consistent with plasmaspheric virtual resonances (PVRs) excited in a magnetohydrodynamic simulation assuming an impulsive energy source. Cross-spectral analysis of the magnetotail flow oscillation and the Pi2 pulsation indicated low coherence between them. These results suggest that the flow oscillation contributed to the Pi2 pulsation as a broadband energy source and that only the spectral components matching the PVR frequencies were detected with well-defined frequencies. Ionospheric currents connected to the PVRs may be responsible for the appearance of the pulsation on the dayside.

1. Introduction

Pi2 pulsations (period = 40–150 s) occur in association with magnetospheric substorms (Saito et al., 1976), pseudo substorm onsets (Kim et al., 2010), and poleward boundary intensifications (Lyons et al., 1999). Although the pulsations are firmly established as an essential element of the substorm phenomenology, there still remain questions as to their source mechanism and propagation mode (e.g., Keiling & Takahashi, 2011). Here the term *source mechanism* refers to a physical process that determines the dominant frequency or frequencies of Pi2 pulsations observed in the magnetosphere and on the ground. Note also that, unless otherwise stated, we use the term Pi2 for pulsations that are detected over a wide range of latitudes and local times either on the ground or in the magnetosphere. Such pulsations are usually detected at $L < 5$ and need to be distinguished from auroral-zone Pi2 pulsations, which exhibit different spatial and spectral properties (Olson & Rostoker, 1975; Samson, 1982).

There is little question that Pi2 pulsations are generated by sudden changes in the state of the magnetotail including generation of bursty bulk flows (BBFs; Angelopoulos et al., 1994) and dipolarizing flux bundles (Liu et al., 2017; Ohtani et al., 2004). A causal relationship between BBFs and Pi2 pulsations was first suggested by Shiokawa et al. (1998), who noted that each Pi2 wave packet detected on the ground followed a compressional magnetic field pulse in the magnetosphere that is attributed to braking of a BBF. Kepko and Kivelson (1999) and Kepko et al. (2001) found waveform similarity between Pi2 pulsations and oscillatory BBFs and proposed

that the former is driven by the latter pulse by pulse. Kepko et al. (2001) attributed Pi2 pulsations in the inner magnetosphere to periodic fast mode pulses that result from braking of periodic BBFs.

While evidence is strong that a Pi2 pulsation is associated with a BBF event occurring somewhere in the magnetotail (Hsu et al., 2012; Kim et al., 2007), it is not clear whether a flow oscillation drives a Pi2 pulsation with the same period. For example, a case study using Geotail and ground magnetometers found little evidence of direct driving of ground Pi2 pulsations by tail flow oscillations (Yamaguchi et al., 2002). More recently, frequency mismatch has been reported between DFB oscillations and Pi2 pulsations (Panov et al., 2014). Also, a statistical analysis indicated that the dominant period of BBF oscillations is ~150 s (Wu et al., 2017), which is longer than the period of Pi2 pulsations except for those occurring during periods of very low *Kp* (Kwon et al., 2013).

A Pi2 source mechanism alternative to pulse-by-pulse driving by BBFs is magnetohydrodynamic (MHD) cavity mode resonance (Saito & Matsushita, 1968; Takahashi et al., 1995; Yeoman & Orr, 1989) or plasmaspheric virtual resonance (PVR; Lee, 1998; Lee & Lysak, 1999). The resonance is driven by external stimuli such as BBFs. The resonance selectively amplifies the external disturbances at frequencies matching those of the MHD fast mode eigenmodes of the inner magnetosphere. Therefore, sinusoidal Pi2 pulsations are excited even when the external disturbance is irregular. Pi2 pulsations often exhibit a sinusoidal waveform lasting many wave periods, and such cases can be better explained by PVRs than BBFs. Many observations in support of PVRs have been presented (Ghamry et al., 2015; Liu et al., 2017; Luo et al., 2011, 2014; Shi et al., 2017; Takahashi et al., 2001, Takahashi, Lee, et al., 2003, Takahashi, Anderson, et al., 2003), but each observation has limited number of measurement points and spatial coverage. Therefore, more observational studies are necessary to quantitatively understand the Pi2-BBF relationship.

Propagation of Pi2 to the dayside also remains to be understood. The PVR mechanism explains the very small phase delay between nighttime and daytime Pi2 pulsations (Nosé et al., 2006; Sutcliffe & Yumoto, 1989). However, absence of dayside magnetic Pi2 signals above the ionosphere led Sutcliffe and Lühr (2010) to propose that toroidal currents flowing between the ionosphere and ground generate dayside Pi2 pulsations on the ground. The role of ionospheric currents in generating low-latitude ground Pi2 was also discussed by Imajo et al. (2017). None of the existing ionospheric Pi2 current models describes how the PVR oscillations are connected to the currents.

In this paper, we examine a Pi2 pulsation event to address generation and propagation of Pi2 pulsations. The event started at ~2226 UT on 8 November 2014 when spacecraft were located both in the flow-braking region and in the inner magnetosphere. Ground magnetometers with a large latitudinal span were located near the local time of the nightside spacecraft. The Pi2 pulsation contained peak spectral power at ~10 and ~19 mHz both in space and on the ground. We compare the observations with multiharmonic PVRs excited in a numerical simulation and find a good match.

The remainder of the paper is organized as follows. Section 2 describes the experiments. Section 3 presents an overview of the event. Section 4 describes magnetospheric observations. Section 5 describes ground observations. Section 6 presents numerical simulation. Section 7 presents discussion, and section 8 concludes the study.

2. Experiments

Data used in this study were acquired with multiple spacecraft and ground magnetometers. The spacecraft experiments include: fluxgate magnetometers on Van Allen Probes, also known as Radiation Belt Storm Probes (RBSP; Kletzing et al., 2013), Time History of Events and Macroscale Interactions during Substorms (THEMIS; Auster et al., 2008), Geostationary Operational Environmental Satellite (GOES; Singer et al., 1996), and Geotail (Kokubun et al., 1994); electric field experiments on RBSP (Wygant et al., 2013) and THEMIS (Bonnell et al., 2008); and plasma experiments on THEMIS (McFadden et al., 2008). The field vectors are expressed using a right-handed magnetic field aligned (MFA) ν-ϕ-μ coordinate system that uses the spacecraft geocentric position vector **R** and the measured (for wave electric fields) or a model (for wave magnetic fields) magnetic field vector $\mathbf{B}_0$ as the reference (Takahashi et al., 2018). In this system, the parallel or compressional

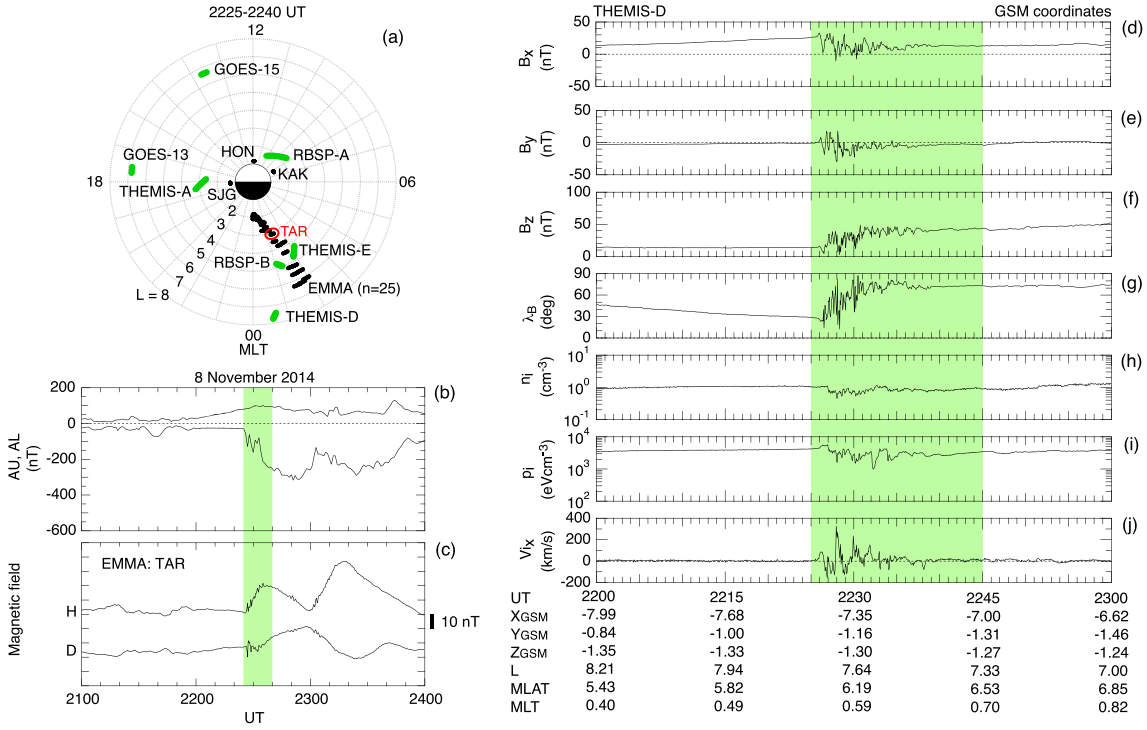

Figure 1. (a) Locations of spacecraft (green) and ground magnetometers (black) in *L*-MLT coordinates at 2225–2240 UT on 8 November 2014. (b) Auroral electrojet indices showing a substorm onset at 2226 UT. The shading indicates the time interval selected for detailed analysis. (c) Magnetic field variations at the Tartu station (TAR, *L* = 3.05) of the EMMA. In the map, the station is highlighted by a red oval. (d–f) Magnetic field components in geocentric solar magnetospheric (GSM) coordinates at THEMIS-D. The shading indicates the same time interval as that highlighted in Figure 1c. (g) Magnetic field elevation angle from the GSM *X*-*Y* plane at THEMIS-D. (h–j) Ion density, pressure, and the GSM *x* component of the bulk velocity at THEMIS-D. GOES = Geostationary Operational Environmental Satellite; RBSP = Radiation Belt Storm Probes; THEMIS = Time History of Events and Macroscale Interactions during Substorms; EMMA = European quasi-Meridional Magnetometer Array; MLT = magnetic local time; MLAT = magnetic latitude; KAK = Kakioka; HON = Honolulu; SJG = San Juan; GSM = geocentric solar magnetospheric.

component $\mathbf{e}_\mu$ is parallel to $\mathbf{B}_0$, the azimuthal component $\mathbf{e}_\phi$ is parallel to $\mathbf{B}_0 \times \mathbf{R}$ and directed eastward, and the radial component $\mathbf{e}_\nu$ is given by $\mathbf{e}_\nu = \mathbf{e}_\phi \times \mathbf{e}_\mu$.

The electric fields from both THEMIS and RBSP were measured using sensors attached to the ends of two pairs of wire booms and processed into spin-fit products with a time resolution of ~3 s for THEMIS and ~11 s for RBSP. The third component of the electric field, which is required to obtain the E_ν and E_ϕ components in MFA coordinates, is obtained using the $\mathbf{E} \cdot \mathbf{B} = 0$ assumption, where **E** and **B** are the electric and magnetic field vectors, respectively. This technique produces reliable results when **B** makes a large angle from the spin plane. This condition was not satisfied at RBSP-B during the Pi2 event. Fortunately, RBSP-B was located near midnight, where the duskward component of **E** in modified geocentric solar ecliptic coordinates (denoted E_{yMGSE}; Rowland & Wygant, 1998) is a good proxy to the westward component $-E_\phi$ in MFA coordinates. Therefore, we use E_ϕ^* (= $-E_{yMGSE}$) to represent the azimuthal (eastward) component of the electric field at RBSP-B.

The ground magnetometers belong to the European quasi-Meridional Magnetometer Array (EMMA) network (Lichtenberger et al., 2013), the U.S. Geological Survey network (Love & Finn, 2011), and the Kakioka observatory (Tsunomura et al., 1994). Data from these sources are provided in 1-s time resolution. We use the horizontal *H* (northward) and *D* (eastward) components of the magnetic field.

3. Event Overview

3.1. Locations of Observations and Geomagnetic Activity

Figure 1 provides background information on the selected Pi2 event, which occurred between 2225 and 2240 UT on 8 November 2014. Observations of this event were made by multiple spacecraft and ground magnetometers at locations shown in Figure 1a using *L* and magnetic local time (MLT) coordinates. The *L* values of the EMMA ground magnetometers were calculated using the corrected geomagnetic latitude based on the International Geomagnetic Reference Field model. The *L* values of the other ground magnetometers

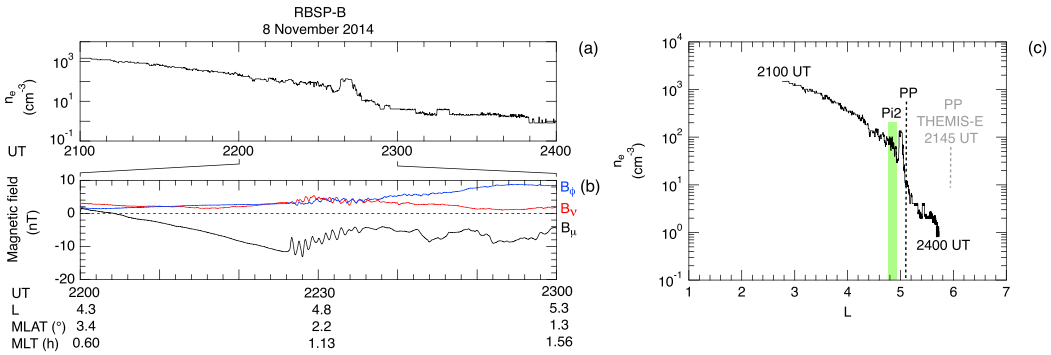

Figure 2. (a) Electron density at RBSP-B. (b) Magnetic field components at RBSP-B expressed in MFA coordinates. The magnitude of the model field has been subtracted from the B_μ component. (c) Electron density plotted as a function of L. The shading indicates where the Pi2 pulsation was detected. The black vertical dashed line labeled "PP" indicates the plasmapause, which is the midpoint of the steep density gradient. The gray vertical dashed line indicates the similarly defined plasmapause using THEMIS-E data. THEMIS-E was moving inward and encountered the plasmapause at 2145 UT. RBSP = Radiation Belt Storm Probes; THEMIS = Time History of Events and Macroscale Interactions during Substorms; MLT = magnetic local time; MLAT = magnetic latitude.

and spacecraft were calculated using a centered dipole. The 0000–0200 MLT sector was well covered by the THEMIS-D, THEMIS-E, and RBSP-B spacecraft and by the EMMA ground magnetometer array. Twenty-five EMMA magnetometers spanning L = 1.57–6.48 were operational at the time of the Pi2 event. Elsewhere, we have GOES-13 and THEMIS-A at dawn and RBSP-A and GOES-15 near noon. We have low-latitude ground magnetometers at Kakioka (KAK), Honolulu (HON), and San Juan (SJG) to monitor Pi2s away from midnight.

A substorm started at 2226 UT. At this time, the *AL* index began to decrease (Figure 1b) and the *H* component at Tartu (TAR) started a midlatitude positive bay with a Pi2 pulsation superposed on it (Figure 1c). Located in the near-Earth magnetotail at $X_{GSM} \sim -7.5R_E$, THEMIS-D observed dipolarization of the magnetic field and oscillatory flow braking (Figures 1d–1j). THEMIS-D was close to the plasmasheet midplane with $Z_{GSM} \sim -1.3R_E$ and to the magnetic equator with magnetic latitude (MLAT) ~6°.

3.2. Plasmapause Location

Plasma mass density affects propagation and mode structures of MHD waves, and it is important to have information on the density in studying Pi2 pulsations. For our event, the electron density (n_e) can be inferred at RBSP-B from plasma wave spectra (Kurth et al., 2015) as shown in Figure 2a. The density is a good proxy to the mass density (ρ) when there is little change of the ion composition with L. If that is not the case, n_e and ρ have different L profiles (Fraser et al., 2005). When the Pi2 pulsation was detected (2226–2235 UT), the spacecraft was located at L = 4.78–4.92, and n_e was in the range 30–80 cm^{-3} (Figure 2b). This places the spacecraft just inward of the plasmapause (Figure 2c), which is defined to be the middle of the steep inward density gradient at L = 5.1 (~2243 UT). Although we do not know where the mass density plasmapause was, we are certain that the spacecraft was located within the mass density plasmasphere because mass density enhancement (oxygen torus) occurs just outside the electron plasmapause (Nosé et al., 2015). THEMIS-E, which was moving inward, encountered the plasmapause (inferred from the spacecraft potential data) at 2145 UT at $L \sim 6$. Therefore, this spacecraft was also in the plasmasphere when the Pi2 pulsation occurred.

Figure 2b shows that B_μ oscillated with amplitudes up to ~4 nT peak to peak, much larger than those of the B_ν and B_ϕ components. The absence of strong transverse wave magnetic field components near the magnetic equator (MLAT ~ 2°) implies that the field line displacement had a mode structure symmetric about the magnetic equator (Sugiura & Wilson, 1964). In the following sections, we present a detailed examination of observations made in the 2225–2240 UT interval.

4. Observations in the Magnetosphere

4.1. Position Dependence

Figure 3 compares the sunward component of the ion bulk velocity (V_{ix}) observed at THEMIS-D (Figures 3a and 3f) with the E_ϕ (E^*_ϕ at RBSP-B; Figures 3b–3e) and B_μ (Figure 3g–3l) components observed closer to the Earth at other spacecraft. The magnitude of the T89c model field (Tsyganenko, 1989) has been subtracted from B_μ. The panels are ordered according to the local time and radial distance of the spacecraft, with nightside

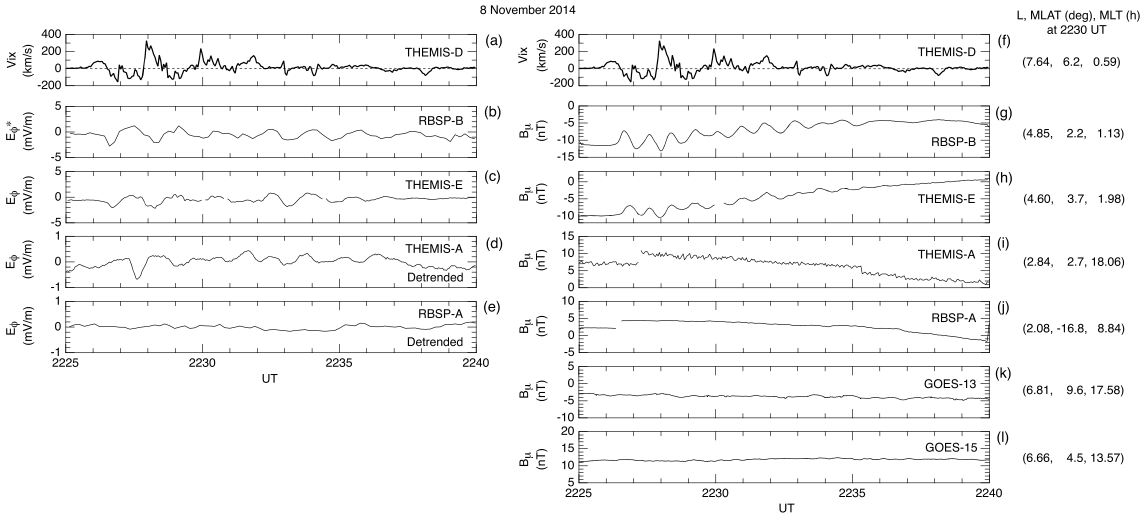

Figure 3. Comparison of the sunward component of the ion bulk velocity (V_{ix}) at THEMIS-D (a, f) and the electric (b–e) and magnetic (g–l) fields of compressional poloidal oscillations at other spacecraft. The linear trend versus UT has been removed from the E_ϕ data from THEMIS-A and RBSP-A. The T89c model field has been subtracted from the magnetic field. Steps seen in the B_μ data from THEMIS-A and RBSP-A are instrumental. GOES = Geostationary Operational Environmental Satellite; RBSP = Radiation Belt Storm Probes; THEMIS = Time History of Events and Macroscale Interactions during Substorms; EMMA = European quasi-Meridional Magnetometer Array; MLT = magnetic local time; MLAT = magnetic latitude.

spacecraft at the top and dayside spacecraft at the bottom. The magnetic coordinates of each spacecraft are shown on the right.

Electric field oscillations are present at RBSP-B and THEMIS-E with very similar waveforms. The oscillations have an amplitude of 2–3 mV/m peak to peak and an average period of ~100 s, not very different from that (~120 s) of the V_{ix} oscillation at THEMIS-D. The similarity between RBSP-B and THEMIS-E is not surprising, because these spacecraft were close to each other with an L separation of ~0.2 and an MLT separation of ~0.9 hr. Nevertheless, the similarity demonstrates that the oscillations are not very localized. An electric field oscillation with a much smaller amplitude (note the different amplitude scale) is visible at THEMIS-A (L = 2.8, MLT = 18 hr). Before 2230 UT, the E_ϕ oscillation at THEMIS-A is out of phase with those seen at RBSP-B and THEMIS-E. After 2230 UT, the period of the E_ϕ oscillation at THEMIS-A becomes ~70 s, which is shorter than that (~100 s) at RBSP-B. There is no indication of such an oscillation at RBSP-A (L = 2.1, MLT = 8.8 hr).

The B_μ plots also show clear oscillations at RBSP-B and THEMIS-E. These spacecraft see nearly identical regular oscillations with a period of ~50 s. The period is approximately half of that of the E_ϕ oscillations. There is no regular ~50 s V_{ix} oscillation at THEMIS-D, which implies that the 50-s oscillation was generated in the inner magnetosphere. The period ratio between the E_ϕ and B_μ oscillations suggests that they are different harmonics (fundamental and second) of standing compressional waves.

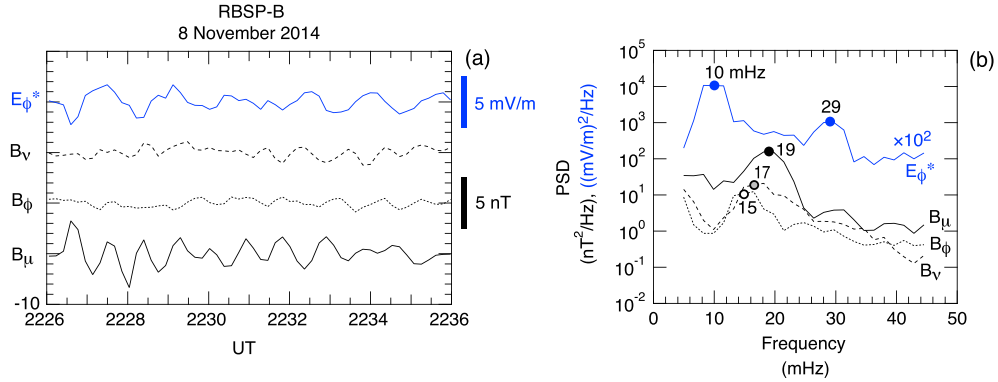

Figure 4. (a) Electric and magnetic field time series at RBSP-B. (b) Power spectral densities computed from the time series. RBSP = Radiation Belt Storm Probes.

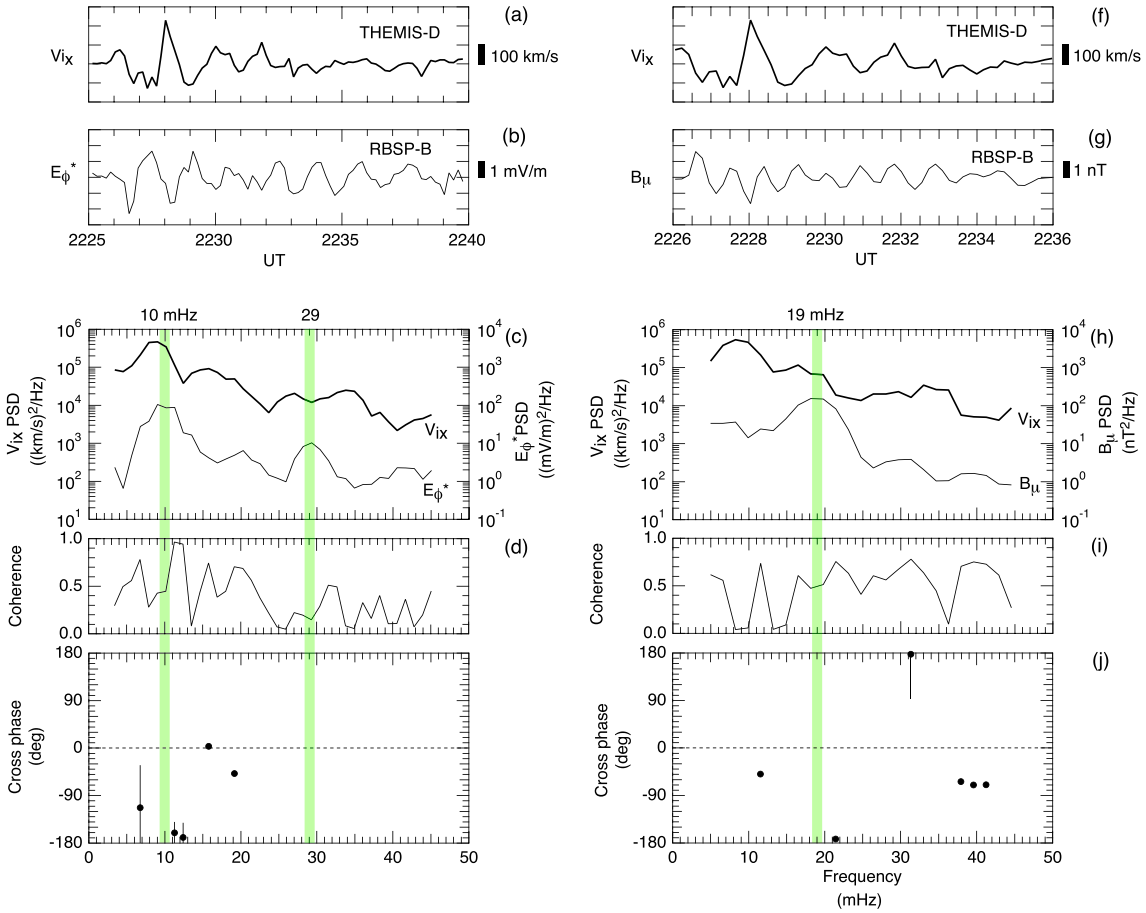

Figure 5. Comparison of bulk flow oscillation at THEMIS-D and ultralow frequency oscillations at RBSP-B. (a) V_{ix} at THEMIS-D. (b) E^*_ϕ at RBSP-B. (c) PSD of V_{ix} and E^*_ϕ. (d) Coherence between V_{ix} and E^*_ϕ. (e) Cross phase between V_{ix} and E^*_ϕ. (f–j) Same as (a–e) but for 2226–2236 UT and B_μ at RBSP-B. RBSP = Radiation Belt Storm Probes; THEMIS = Time History of Events and Macroscale Interactions during Substorms; PSD = power spectral density.

4.2. Wave Mode at RBSP-B

Figure 4 shows the time series and power spectral density (PSD) of four field components at RBSP-B for a 10-min interval covering the main part of the Pi2 event. Throughout this paper, computation of spectral parameters is done using the Fourier transform method (e.g., Bendat & Piersol, 1971; Green, 1976), and the input time series for the transform (e.g., Figure 4a) is detrended by removing a quadratic function fitted to the time series by the least squares method. The E^*_ϕ PSD exhibits peaks at 10 and 29 mHz, and the B_μ PSD exhibits a peak at 19 mHz (Figure 4b). The transverse magnetic field components B_ν and B_ϕ oscillate at intermediate frequencies of 17 and 15 mHz, respectively. Our interpretation of these frequency characteristics is that the E^*_ϕ and B_μ oscillations are caused by fast mode waves spanning many L shells, whereas the B_ν and B_ϕ oscillations are caused by standing Alfvén waves localized in L. We do not consider that the 2-mHz frequency difference between the B_ν and B_ϕ spectral peaks is significant given the short duration of the oscillations and the broadness of the spectral peaks.

We have two reasons to believe that the standing Alfvén waves were excited at the second harmonic. The first reason is that the RBSP-B was very close to the magnetic equator, where the fundamental wave has a node of the B_ν and B_ϕ components. The second reason is that the observed frequencies (15–17 mHz) are higher, by a factor of ~2, than that of the estimated fundamental toroidal wave frequency ~8 mHz. Here the estimation was done using the toroidal wave equation of Cummings et al. (1969) assuming that the mass density is constant all along the magnetic field line and that H^+ is the only ion constituent. The mass density is specified using the observed electron density (n_e), which was ~70 cm^{-3} during the observation shown in Figure 2c. In the presence of heavy ions, the toroidal wave frequency becomes lower. This brings the ratio between the fundamental and second harmonic frequencies to >2, as shown by Cummings et al. (1969).

4.3. Relation to Flow Oscillation

Figure 5 compares the V_{ix} oscillation at THEMIS-D with the E_ϕ^* and B_μ oscillations at RBSP-B. The left column (Figures 5a–5e) shows the V_{ix} and E_ϕ^* time series and corresponding spectral parameters. The V_{ix} oscillation produces a spectral peak at 9 mHz, which is close to the 10-mHz peak in the E_ϕ^* spectrum (Figure 5c). However, the V_{ix}-E_ϕ^* coherence at 9–10 mHz is only ~0.5 (Figure 5d), too low to define reliable cross phase (Figure 5e). The same can be said of the B_μ versus V_{ix} results at 19 mHz (Figures 5f–5j). We conclude that there is little evidence that the V_{ix} oscillation determined the frequency of the E_ϕ^* and B_μ oscillations observed at RBSP-B.

5. Observations on the Ground

In this section, we examine the relationship between oscillations observed in the inner magnetosphere and on the ground.

5.1. Nightside Observations

We first examine the relationship between the E_ϕ^* and B_μ oscillations detected at RBSP-B and oscillations detected on the nightside by the EMMA in the 2226- to 2236-UT interval. Figure 6a shows the geographic coordinates of the 25 EMMA magnetometers along with the footprint of RBSP-B given by the T89c model. The EMMA stations cover an L range of 1.57–6.48, and their longitudinal distances from the RBSP-B footprint are $< 25°$. Recalling that the plasmapause was located at $L \sim 5$ according to Figure 2c, we mark stations located at $L < 5$ using black circles and stations located at $L > 5$ using red circles. The E_ϕ^* and B_μ time series from RBSP-B (Figure 6b) and the corresponding power spectra (Figure 6e), repeated from Figure 4, are included for comparison with the EMMA data.

On the ground, oscillations appear both in the H and D components, and their properties change across $L \sim 5$. Figures 6c and 6d show that in both H and D the oscillation amplitude is of the order of 1–10 nT and the waveform changes little from one station to another at $L < 5$, whereas the amplitude is of the order of 10–100 nT and the waveform changes from one station to another at $L > 5$. At $L < 5$, the D component amplitude decreases toward lower L, a behavior not seen in the H component. This component dependence has been reported in previous studies (Li et al., 1998; Yumoto et al., 1994), and Allan et al. (1996) have provided a theoretical explanation to it.

In addition, Figure 6f reveals that the H oscillations at $L < 5$ contain spectral power peaking at 10, 19, and 29 mHz, matching the spectral peaks found at RBSP-B in the E_ϕ (10 and 29 mHz) or the B_μ (19 mHz) component. No such spectral peaks occur at EMMA stations located at $L > 5$, confirming the previously reported difference between Pi2-band ground pulsations at low and high latitudes (Olson & Rostoker, 1975; Samson, 1982). The ground D components at $L < 5$ also exhibit spectral peaks at or near the three frequencies (Figure 6g). However, the peaks in the D spectra are less prominent and tend to become weak as L decreases.

Figure 7 illustrates the L dependence of spectral parameters computed for the H and D oscillations observed at EMMA at 2226–2236 UT. Figure 7a is the electron density L profile from RBSP-B (repeated from Figure 2c), which facilitates visual understanding of where the ground magnetometers are relative to the plasmapause. The green vertical shading indicates the location of RBSP-B at the time of the Pi2 pulsation. Figure 7b shows the H and D PSD evaluated at 9.9 mHz. Figures 7c and 7d show the coherence and phase of H and D with respect to E_ϕ^* at RBSP-B, also evaluated at 9.9 mHz. Figures 7e–7h are the same as Figures 7a–7d except that the B_μ component at RBSP-B is used as the reference for the coherence and cross phase, and the spectral parameters are evaluated at 19.8 mHz.

We consider the H component first. At both frequencies, the H-component PSD is nearly constant from L = 1.6 to L = 4, and it increases with L at $L > 4$ (Figures 7b and 7f). Also at both frequencies, the space-ground coherence is high (>0.9) at 1.6–3.8 and stays low (<0.7) at higher Ls except for the highest L, 6.48 (Figures 7c and 7g). The E_ϕ^*-H cross phase is nearly constant at ~90° for $L < 4$ (Figure 7d). Similarly, the B_μ-H cross phase is nearly constant at ~180° for $L < 3.5$ (Figure 7h). The L profile of the E_ϕ^*-H cross phase is consistent with previous studies, including a statistical study using Kakioka ground magnetometer data and electric field data from the Combined Release and Radiation Effects Satellite (Takahashi, Lee, et al., 2003), a multispacecraft study of a single event (Luo et al., 2011), and a THEMIS and Super Dual Auroral Radar Network study of a single event (Shi et al., 2017). The L profile of the B_μ-H cross phase 19.8 mHz (second harmonic) is new. In a study that examined Pi2 signals in E_ϕ^* and B_μ (Takahashi, Lee, et al., 2003), the authors focused on events that both components

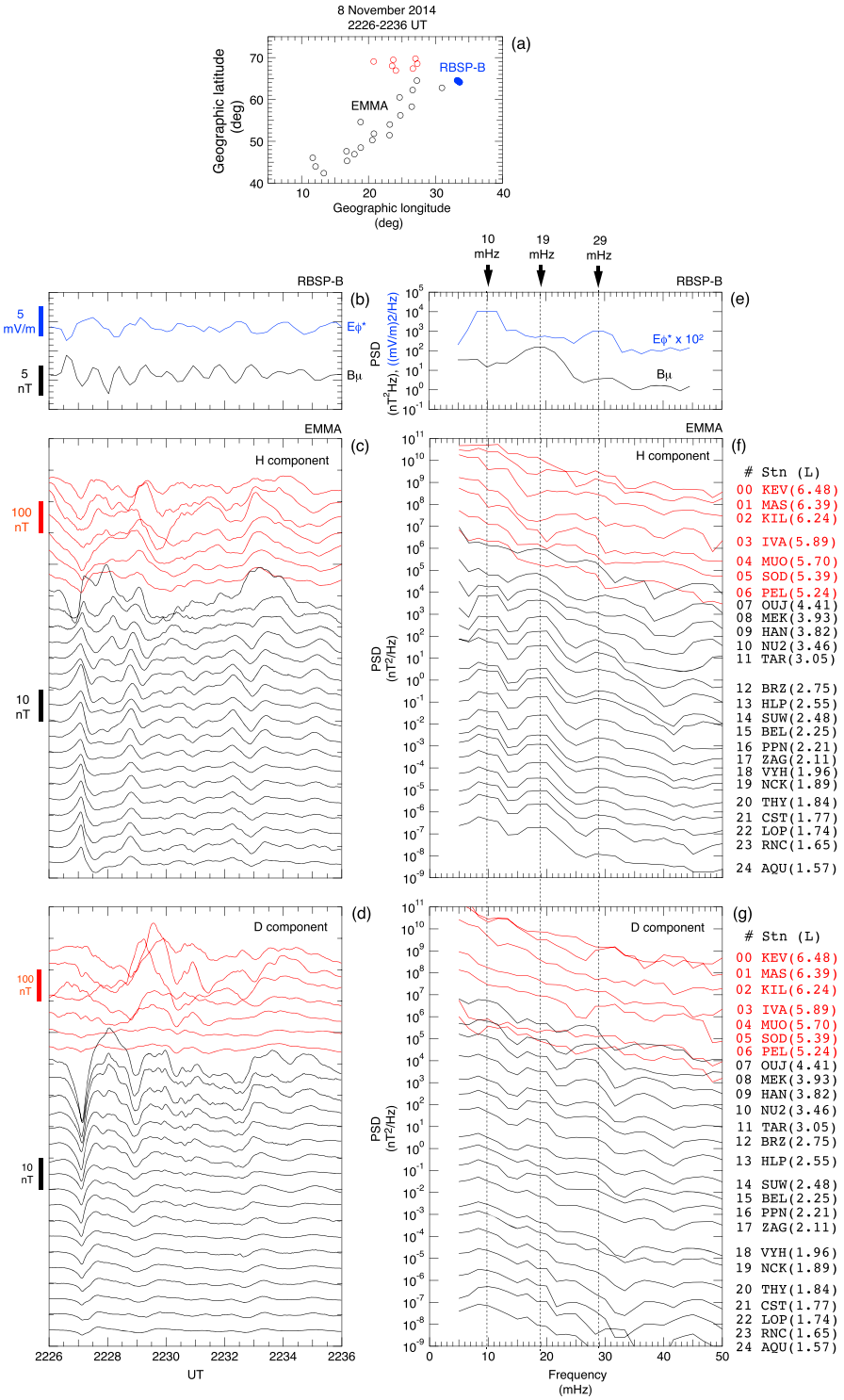

Figure 6. (a) Geographic coordinates of the EMMA stations (open circles) and the RBSP-B footprint (blue dots) for 2226–2236 UT. Stations located at $L < 5$ are shown in black, and stations located at $L > 5$ are shown in red. (b–d) Time series plots of selected field components from RBSP-B and EMMA. Each time series has been detrended by removing the quadratic function fitted to the original. The L value of the EMMA stations increases from bottom to top. The amplitude scale for the EMMA data changes across $L = 5$. (e–g) PSD calculated from the time series data. For EMMA, the baseline for the PSD traces is shifted by a factor of 5 from one station to the next to avoid overlap. Arrows point to spectral peaks at 10, 19, and 29 mHz. EMMA = European quasi-Meridional Magnetometer Array; RBSP = Radiation Belt Storm Probes; PSD = power spectral density.

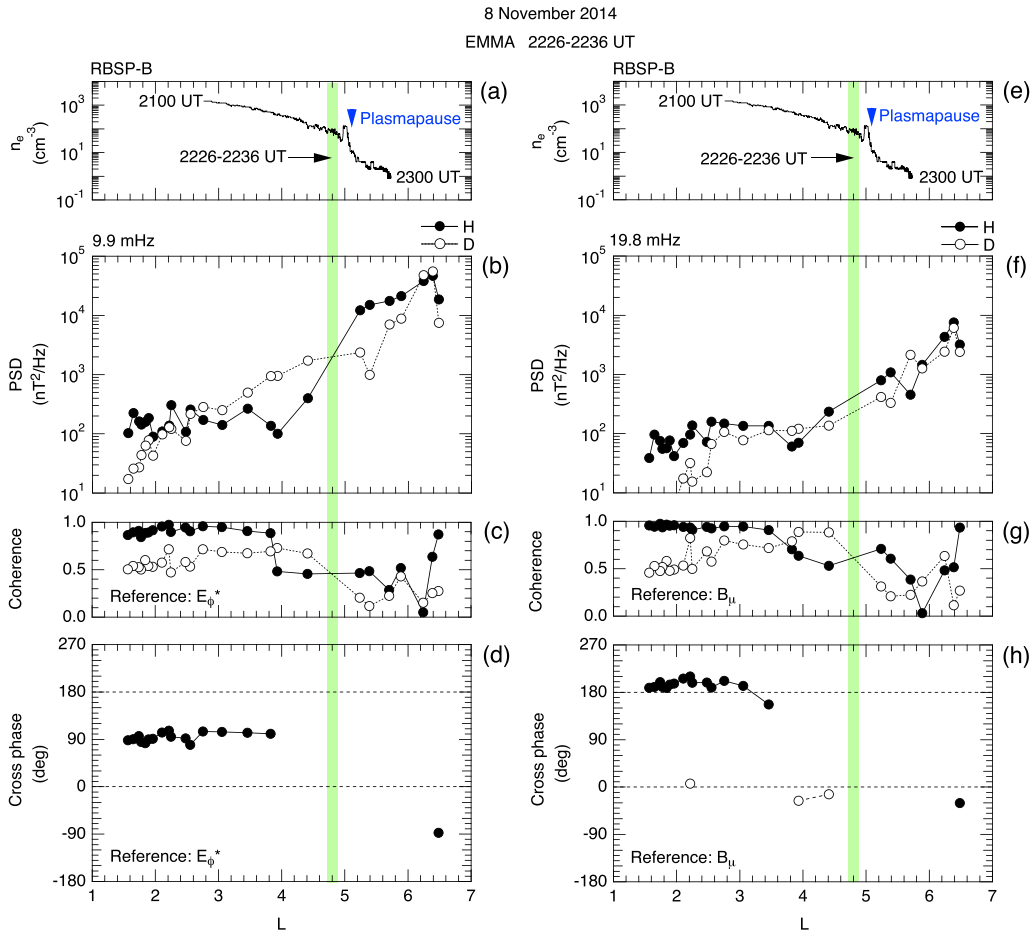

Figure 7. (a) Electron density at RBSP-B repeated from Figure 2c. (b–d) *L* dependence of the spectral parameters of *H* and *D* oscillations at EMMA detected at 2226–2236 UT and evaluated at 9.9 mHz. The coherence and cross phase are computed using the E_{ϕ}^{*} component at RBSP-B as the reference. The cross phase is shown at frequencies with coherence >0.8. Positive cross phase means that the ground signal leads the spacecraft signal. (e–h) Same as (a–d) except the spectral parameters are evaluated at 19.8 mHz and the B_{μ} component at RBSP-B is used as the reference for the coherence and cross phase. EMMA = European quasi-Meridional Magnetometer Array; RBSP = Radiation Belt Storm Probes; PSD = power spectral density.

exhibited a common frequency. In a study (Luo et al., 2011) that examined multifrequency Pi2 events that are similar to the event reported here, only one ground station was used and no *L* profile of the phase of ground pulsations was presented. We will discuss the *L* dependence of the B_{μ}-*H* relationship in section 6.

The spectral parameters for the *D* component show differences from the *H* component. Consider the 9.9-mHz results first. The *D*-component PSD increases more or less linearly with *L* in logarithmic scale at all *L*, in contrast to the *H*-component PSD, which varies little at $L < 4$ (Figure 7b). In addition, the E_{ϕ}^{*}-*D* coherence is lower than the E_{ϕ}^{*}-*H* coherence except at $L = 3.9$, $L = 4.4$, and $L = 6.2$ (Figure 7c). We find qualitatively the same features in the 19.8-mHz results (Figures 7f–7g).

5.2. Observations on the Dayside

The Pi2 pulsation was detected on the dayside with low-latitude ground magnetometers. Detection of the dayside pulsation was possible because of the absence of strong compressional ultralow frequency (ULF) waves propagating from the solar wind. Figure 8a shows that the pulsation occurred when Geotail was located in the solar wind and GOES-15 was located in the postnoon sector approximately over HON. During the ~1-hr interval centered on the Pi2 event marked by a vertical arrow at the bottom of Figure 8e, the interplanetary magnetic field (IMF) magnitude B_t was ~6 nT (Figure 8b), and the IMF cone angle θ_{xB} (=$\cos^{-1}(|B_x|/B_t)$, Figure 8c) was mostly >60°, where B_x is the component along the Sun-Earth line. The high-frequency fluctuations seen in B_t and θ_{xB} indicate entries of the spacecraft into the ion foreshock. When θ_{xB} is large, the ion

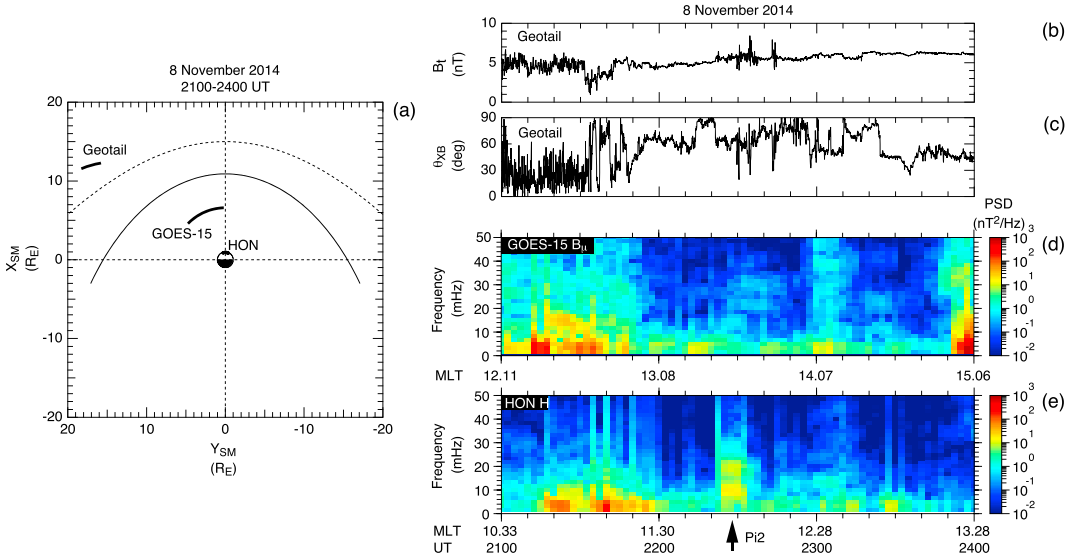

Figure 8. (a) Location of spacecraft and ground station in the Solar Magnetospheric coordinate *X*-*Y* plane. (b, c) Magnitude and cone angle of the IMF measured by Geotail. (d) Dynamic spectra of the B_μ component at GOES-15. (e) Dynamic spectra of the *H* component at HON. GOES = Geostationary Operational Environmental Satellite; HON = Honolulu; MLT = magnetic local time.

foreshock upstream of the subsolar magnetopause is generally free of strong upstream ULF waves (Fairfield, 1969), and compressional Pc3–Pc4 (7–100 mHz) magnetic field oscillations are suppressed in the dayside magnetosphere (Yumoto et al., 1985). This IMF effect explains the low level of the B_μ spectral power at GOES-15 at 2200–2300 UT (Figure 8d). The Pi2 pulsation that is seen in the *H* component power at HON (Figure 8e) is absent at GOES-15. These observations indicate that the Pi2 pulsation did not propagate to GOES-15.

Figures 9a–9e compare the B_μ component at RBSP-B and the *H* components at low-latitude ($L < 2$) ground stations located at midnight (L'Aquila, AQU), dusk (SJG), dawn (KAK), and noon (HON). The midnight station (AQU) detected oscillations with a more complex waveform than at RBSP-B. However, by following the

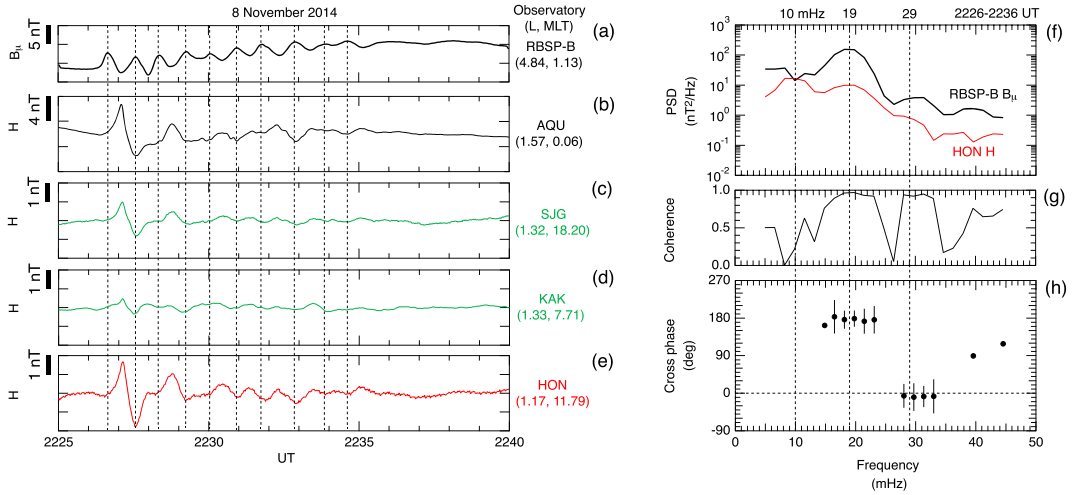

Figure 9. (a) B_μ component at THEMIS-B with the magnitude of the T89c model field subtracted. (b–e) Detrended *H* components at four low-latitude stations. The *L* value calculated from the corrected geomagnetic latitude and the dipole MLT at 2230 UT are shown in parentheses below the station code. Vertical dashed lines are drawn through the frequencies of the peaks found in the E^*_ϕ and B_μ PSDs shown in Figure 4b. (f–h) Spectral parameters computed from the B_μ component at RBSP-B and the *H* component at HON. RBSP = Radiation Belt Storm Probes; MLT = magnetic local time; PSD = power spectral density; AQU = LŠAquila; SJG = San Juan; KAK = Kakioka; HON = Honolulu.

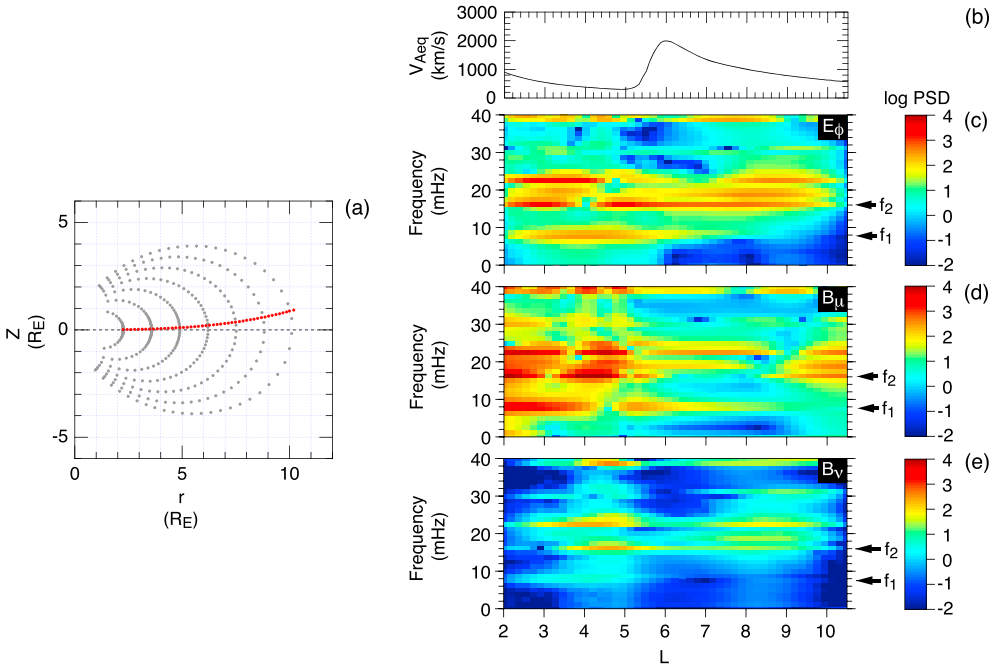

Figure 10. Numerical simulation of magnetohydrodynamic waves in a dipole magnetic field. (a). Grid points on selected dipole field lines (gray dots) and grid points at which power spectral density (PSD) is calculated (red dots). (b) *L* profile of the equatorial Alfvén velocity. (c–e) PSD of field components associated with compressional poloidal waves. Arrows point to the fundamental and second harmonic frequencies.

vertical dashed lines drawn through the peaks of B_μ, we confirm the presence of an *H* oscillation that is ~180° out of phase with B_μ. This phase delay is seen at the other three stations as well, including the noon station HON (Figures 9c–9e). Apparently, low-latitude Pi2 pulsation propagated from midnight to noon with very little phase delay similar to Pi2 events reported by Nosé et al. (2006). The power spectrum of HON *H* exhibits a peak at 19 mHz, matching the strong peak in the B_μ spectral peak (Figure 9f). At this frequency, the B_μ-*H* coherence is high and the cross phase is ~180°, consistent with the phase delay noted in the time series plots. The *H* spectrum exhibits another peak at 10 mHz. This peak is absent in the B_μ spectrum but is present in the E_ϕ^* spectrum shown in Figure 4b. To summarize, the ground Pi2 pulsation observed at noon contained the two spectral components that appeared separately in B_μ and E_ϕ^* at RBSP-B. A qualitatively identical space-ground relationship has been reported by Takahashi, Anderson, et al. (2003) and Luo et al. (2011), but in their studies both the spacecraft and the ground magnetometers were located in the midnight sector. These authors attributed the observations to simultaneous excitation of the fundamental and second harmonic cavity mode oscillations.

6. Numerical Simulation

We compare the observed Pi2 pulsation with numerically simulated MHD oscillations. The simulation was run using the code described by Lee and Lysak (1999). The simulation uses 98 × 98 × 98 grid points in the *L*-MLT-MLAT space. Figure 10a shows selected grid points. The model mass density has a realistic plasmasphere structure, which produces the radial profile of the equatorial Alvén velocity shown in Figure 10b. The profile shows a positive slope from $L = 5$ to $L = 6$ corresponding to the plasmapause density gradient. The plasmapause location is close to the observation shown in Figure 2c. The outer boundary conditions and the spatial and temporal specification of the source disturbance are the same as Lee and Lysak (1999). We show results obtained by imposing the ionospheric boundary condition $(\mu_0 V_A \Sigma_P)^{-1} = 0.3$, where μ_0 is the permeability of free space, V_A is the Alfvén velocity, and Σ_P is the height-integrated ionospheric Pedersen conductivity.

Figures 10c–10d show the spectral power of the simulated E_ϕ, B_μ, and B_ν oscillations as a function of *L* and frequency. The selected field components were sampled in the midnight meridian plane slightly above the

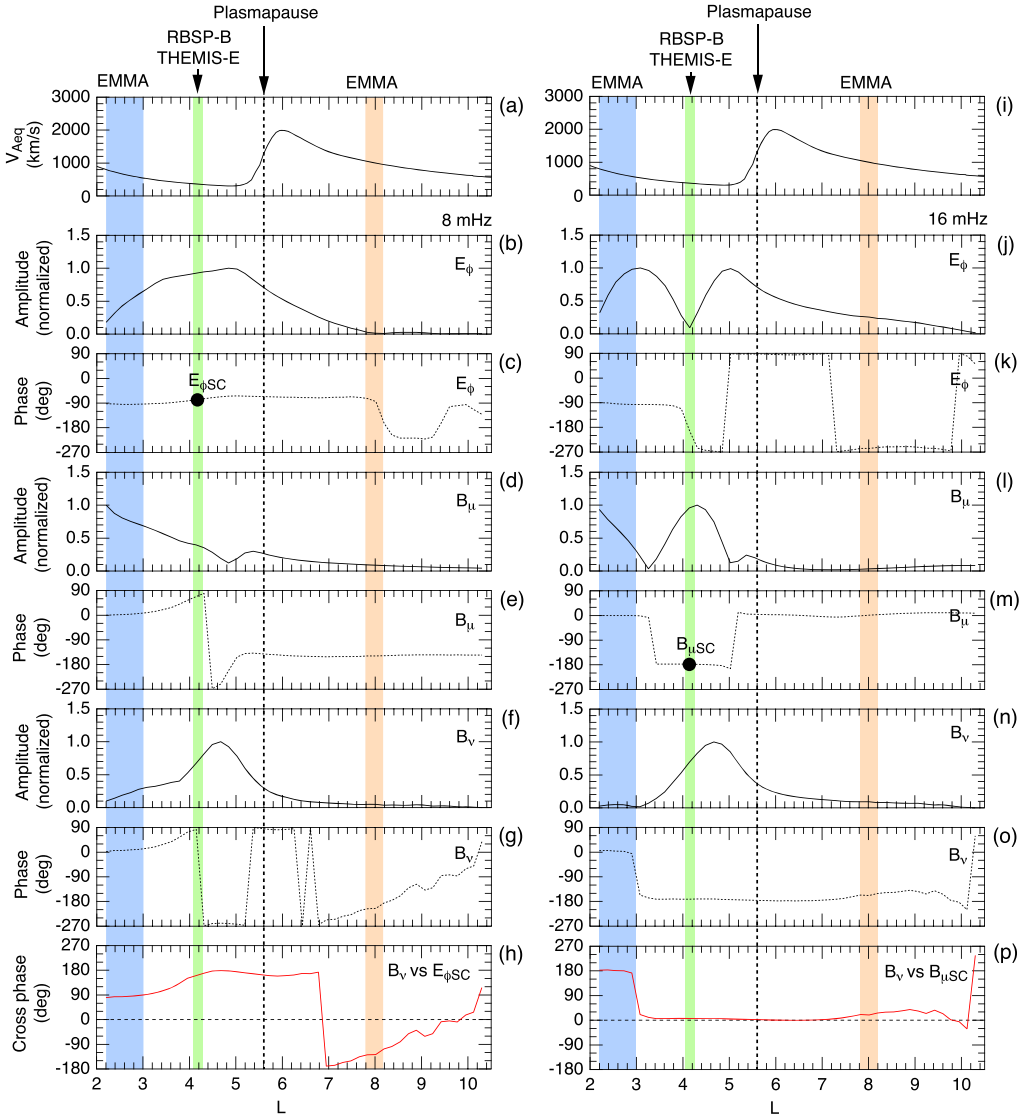

Figure 11. *L* profiles of variables from the magnetohydrodynamic simulation shown in Figure 10. The vertical dashed lines indicate the center of the plasmapause density gradient. The green shading at $L \sim 4.1$ (B_μ node of the 16-mHz mode) indicates the location that can explain the observations at RBSP-B and THEMIS-E. The *L* domains shaded in blue and orange correspond to the EMMA stations at which *H*-component pulsations have high coherence with oscillations detected at the spacecraft, as shown in Figure 7. (a) Equatorial Alfvén velocity. (b–g) Amplitude and phase of the poloidal components evaluated at 8 mHz. The amplitude is normalized to the maximum value. The phase is defined relative to the B_μ oscillation at the inner edge ($L = 2.0$) of the simulation domain. (h) Phase of B_ν relative to that of E_ϕ at the spacecraft (black dot in panel c) . (i–o) Same as (a–g) but for 16 mHz. (p) Phase of B_ν relative to that of B_μ at the spacecraft (black dot in panel m). RBSP = Radiation Belt Storm Probes; THEMIS = Time History of Events and Macroscale Interactions during Substorms; EMMA = European quasi-Meridional Magnetometer Array.

magnetic equator at the red grid points shown in Figure 10a. The discrete horizontally extended structures visible in the spectra correspond to harmonics of the PVR. The lowest mode occurs at 8 mHz, and the next lowest mode occurs at 16 mHz. These are identified to be the fundamental and second harmonic PVR modes, respectively. The frequencies, referred to as "f_1" and "f_2," are only slightly lower than the observed frequencies 10 and 19 mHz and provide a first piece of evidence for PVR oscillations in the real magnetosphere.

The radial mode structure of the simulated PVRs is also consistent with the observations. Figure 11 shows the radial mode structures of E_ϕ, B_μ, and B_ν. The Alfvén velocity profile (Figures 11a and 11i) is repeated from Figure 10b as a reference. For each field component, the amplitude is obtained by taking the square root of its PSD shown in Figure 10 at the selected frequencies. The amplitude is normalized to the maximum value

across the L domain of the simulation. The phase is defined relative to the B_μ oscillation at the inner boundary $L = 2$. At $L < 3$, B_μ and ground H oscillate in phase during Pi2 pulsation events (e.g., Takahashi et al., 1992), so the phase of H can be used as proxy for the phase of B_μ in the low-L region.

The left column of Figure 11 shows the mode structure at the fundamental frequency f_1 (= 8 mHz). The E_ϕ component has a peak (antinode) at $L = 4.8$ (Figure 11b), which is colocated with the minimum (node) of the B_μ component (Figure 11d). The phase of E_ϕ stays close to −90° from $L = 2$ to $L = 8$. The phase of B_μ is ∼0 at $L < 3.5$, rapidly changes across the node, and stays near −180° at $L > 5$ (Figure 11e). As a consequence, the relative phase between E_ϕ and B_μ is $\sim \pm 90°$, except near the B_μ node, as expected for radially standing fast mode waves. B_ν exhibits an amplitude structure (Figure 11f) similar to that of E_ϕ, and, at $L < 4$, a phase structure (Figure 11g) similar to that of B_μ. However, at higher L, the phase of B_ν differs from that of B_μ.

We include Figure 11h to facilitate a comparison of the simulation and the observation shown in Figure 7d. To generate Figure 7d, we determined the phase of H at multiple ground stations relative to the phase of E^*_ϕ at a single point in space. For Figure 11h, we do the same using B_ν at multiple grid points and E_ϕ at a single grid point. The choice of B_ν in this case is based on the theoretical prediction that, in the northern hemisphere, the B_ν oscillation associated with a fast mode wave produces a ground H oscillation without phase delay (Allan et al., 1996; Nishida, 1978). According to this prediction, the E_ϕ-B_ν cross phase shown in Figure 11h is equivalent to the E^*_ϕ-H cross phase shown in Figure 7d. In both figures, the cross phase stays near 90° in a low-L region ($L < 4$ in Figure 7d and $L < 3$ in Figure 11h, highlighted by shading in blue). The cross phase changes as L increases, both in the simulation and observation. For example, at $L \sim 8$ (highlighted by shading in orange), the cross phase from the simulation is close to −90°, consistent with the cross phase ∼−90° found in Figure 7d at the station located at $L = 6.48$. In the observation, we cannot determine the cross phase around the plasmapause because of the low satellite-ground coherence.

The right column of Figure 11 shows the mode structure at the second harmonic frequency f_2 (= 16 mHz). For this mode, a node of E_ϕ and an antinode of B_μ appear at $L \sim 4.1$. We consider that RBSP-B and THEMIS-E were very close to this location during the Pi2 wave event, because the E^*_ϕ and E_ϕ spectra at these spacecraft exhibit a peak at 10 mHz (fundamental frequency) but not at 19 mHz (second harmonic frequency), whereas the B_μ spectra exhibit the opposite. The B_ν component has a node at $L = 3$ (Figure 11n), which is colocated with an antinode of E_ϕ (Figure 11j). Accordingly, the B_ν phase changes from ∼0 to ∼−180° across $L = 3$ (Figure 11o).

Figure 11p shows the phase of B_ν relative to the phase of B_μ at the spacecraft location. This phase profile can be directly compared with the observational result shown in Figure 7h. Both the simulation and observation show cross phase values close to 180° in the low-L region. In addition, the cross phase value of ∼−30° obtained in the observation at $L = 6.48$ (Figure 7h) is not far from the value of ∼30° that is obtained from the simulation at $L = 8$ (Figure 11p).

There are observations that the PVR simulation does not explain. First, in the observation, the satellite-ground coherence is low around the plasmapause, including the L shell of the spacecraft. Second, the amplitude of the observed H oscillations increases with L outside the plasmapause, in contradiction to the decrease observed in the simulated B_ν component. This discrepancy might be explained by an ionospheric effect. However, we leave investigation of this problem to future studies.

7. Discussion

7.1. Interpretation of the 8 November 2014 Pi2 Event

Our interpretation of the Pi2 event on 8 November 2014 is schematically summarized in Figure 12. The figure is a modified version of conceptual models presented previously on generation and propagation of Pi2 pulsations (Imajo et al., 2017; Kepko et al., 2001; Liu et al., 2017; Nishimura et al., 2012; Shiokawa et al., 1998; Sutcliffe & Lühr, 2010). The first process that leads to excitation of a Pi2 pulsation in the inner magnetosphere ($L < 5$) is generation of a bursty bulk (Angelopous et al., 1994). As the flow approaches the inner magnetosphere, it brakes and generates an earthward propagating fast mode pulse (Liu et al., 2017; Shiokawa et al., 1998). This pulse excites PVRs (Lee & Lysak, 1999). The spectrum of the incoming fast mode wave can have a peak away from the PVR frequencies, but the peak needs to be broad enough to cover multiple PVR frequencies. Excitation of standing fast mode waves by an impulsive source disturbance, which has a broad spectrum, has been confirmed in both simulation and observation (e.g., Takahashi et al., 2018). The quasiperiodic flow oscillation detected by THEMIS-D (Figure 1j) can be taken to be a series of impulses, with each impulse behaving like

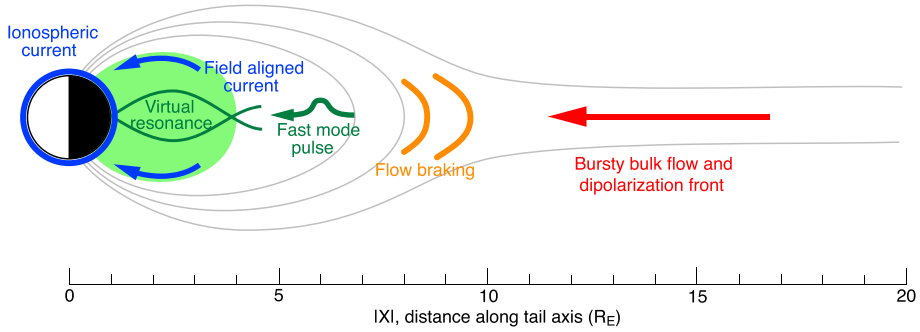

Figure 12. Illustration of Pi2 generation mechanisms proposed in the literature. See text for explanation.

a single pulse applied on the outer boundary in the numerical simulation. Both the propagating fast mode pulse and the PVRs are attenuated on the dayside, so that they cannot be detected by spacecraft located near noon in the inner magnetosphere.

To account for dayside Pi2 pulsations, we need an additional mechanism. Propagation of Pi2s to the dayside is possible if the Pi2 signal is carried by a current system consisting of field-aligned currents (FACs) on the nightside and ionospheric currents that are connected to the FACs and extend to the dayside (Imajo et al., 2017; Sutcliffe & Lühr, 2010). Unlike in the model proposed by Imajo et al. (2017) and Sutcliffe and Lühr (2010), the FACs in our model result from coupling of the Alfvén mode to the PVR. This coupling may or may not be field line resonance (Kivelson & Southwood, 1986). Fast mode and Alfvén mode are always coupled in the inhomogeneous magnetosphere when the modes have a finite azimuthal wave number (Chen & Hasegawa, 1974; Southwood, 1974).

7.2. Comparison With Previously Reported Flow-Driven Pi2 Pulsations

The main result of the present study is that the inner magnetosphere establishes radially standing fast mode waves or PVRs and that the frequencies of the waves depend on the mass density structure (e.g., the plasmasphere). The PVRs are excited by external disturbances that propagate into the magnetosphere as fast mode pulses. In this regard, we agree with existing Pi2 models that consider the pulses as the driver of inner magnetosphere Pi2s. However, as opposed to models in which the fast mode pulses are the cause of individual peaks of the Pi2 time series (e.g., Kepko et al., 2001), we consider that the fast mode resonances (PVRs) play a crucial role in determining the frequencies of Pi2 pulsations observed in the inner magnetosphere and at low-latitude ground stations. Sunward propagation of fast mode waves maintaining the frequency contents of BBFs or flow braking is certainly possible if there is no obstacle (the Earth) in the path of the waves. In fact, Liu et al. (2017) reported such propagation using observations with spacecraft located near dawn. However, the same authors also reported evidence of standing fast mode waves near midnight.

In our event, evidence for standing fast mode waves is strong. The evidence includes the spectral mismatch between magnetotail flow oscillations at THEMIS-D and Pi2 pulsations in the inner magnetosphere observed at RBSP-B (Figure 5) and the constant phase of ground *H*-component Pi2 pulsations over a range of *L* (Figure 7) at both of the two dominant frequencies f_1 and f_2. If fast mode pulses are launched toward the Earth, it is inevitable that at least part of the pulse energy is reflected back toward the tail, and if the inner magnetosphere has a density structure (the plasmapause) to reflect or trap fast mode waves, radially standing waves should be established. Strong evidence that the inner magnetosphere can sustain radially standing fast mode waves was recently presented from an RBSP study of dayside ULF waves excited by an interplanetary shock (Takahashi et al., 2018).

If the BBF frequency matches the PVR frequency, there will be a high degree of coherence between BBF and PVR waveforms. However, sinusoidal BBF oscillations are not required to drive sinusoidal Pi2 pulsations because PVR is capable of enhancing externally applied broadband pulses at discrete frequencies. We recognize that there are Pi2 pulsations with very irregular waveforms. In these cases, the pulsations could be directly driven by fast mode pulses. It may be the case that directly driven Pi2 pulsations prevail if the spectrum of fast mode pulses does not cover the PVR frequencies. This situation may occur when the rise time of the pulse is much longer than the fundamental period of the PVR. Slow rise time means a power spectrum that has a low

cutoff frequency. If the cutoff frequency is lower than the fundamental frequency of the PVR, the plasmasphere cannot find fast mode spectral components to resonate with. The fact that we found a strong PVR mode at both fundamental and second harmonic frequencies implies that the fast mode impulse had a rise time shorter than ~50 s, which is the reciprocal of the frequency (~20 mHz of the second harmonic of the PVR).

7.3. Ground Observations at $L > 4$

The high satellite-ground coherence at the highest L (on the ground) seen at both frequencies (Figures 7c and 7g) merits attention. A simple explanation for this result is that the high-L oscillations are directly driven by a source located at high L (e.g., Nishimura et al., 2012). However, this is inconsistent with the low coherence between V_{ix} and E^*_ϕ and between V_{ix} and B_μ shown in Figure 5, although one could argue that there was another channel of BBFs that drove the Pi2 pulsations in the inner magnetosphere. An alternative explanation is that PVR extended beyond the plasmasphere to $L\sim$ 6.5. According to numerical simulation, this is entirely possible, as Figure 10 shows. Also, evidence of PVR outside the plasmasphere has been reported in a study that used data from the polar-orbiting Dynamics Explorer 1 spacecraft (Teramoto et al., 2011).

Whether one adopts the PVR model or the BBF model, an important question to ask is why the space-ground coherence is low at $L = 4–6$. RBSP-B, located at $L \sim 5$, detected well-defined dual-frequency Pi2 oscillations, whereas ground magnetometers located near the footprint of the spacecraft did not. A possible reason for this observation is that ground magnetic field variations were affected by currents flowing in the ionosphere. Precipitation of auroral particles can time modulate the ionospheric conductivity, and the particles carry currents into and out of the ionosphere. Another possibility is the influence of local FLRs. FLRs can be simultaneously excited with fast mode Pi2 waves (Keiling et al., 2003; Takahashi et al., 1996), and if they propagate to the ground, they can mask ground pulsations that originated from fast mode Pi2.

7.4. Current System for Dayside Pi2

Sutcliffe and Lühr (2010) suggested that dayside Pi2s are produced by currents flowing between the ionosphere and the ground and that the currents are connected to the substorm current wedge via FACs flowing on the nightside. This mechanism could explain our dayside observations as well. To account for our observations, however, the current system needs to be connected to the region of PVRs, not to the auroral zone. In an inhomogeneous magnetosphere, fast mode and Alfvén mode are always coupled and it is possible for PVRs to drive FACs in the plasmasphere. A quantitative model thus needs to incorporate the coupling between PVR and FAC using MHD equations, and then the FAC needs to be connected to the ionospheric currents self-consistently. Existing models for the ionospheric Pi2 current system (Imajo et al., 2017; Sutcliffe & Lühr, 2010) do not include source mechanism of the Pi2 waves, so further modeling efforts are necessary.

8. Conclusions

We have studied the spatial and spectral properties of a Pi2 pulsation event using data from multiple spacecraft and ground magnetometers. The event was associated with a flow-braking oscillation detected in the midnight sector by THEMIS-D just outside the geostationary orbit when RBSP-B and THEMIS-E were also in the midnight sector within the plasmasphere and above the EMMA ground magnetometer array. Propagation of the pulsation to other local times was confirmed by low-latitude ground magnetometers. This distribution of measurement points in the midnight sector allowed us to discuss the relationship between the flow oscillation and Pi2 pulsation and the spatial mode structure of the electric and magnetic fields of the pulsation. The observations were compared with numerically simulated PVR oscillations. Our findings are summarized as follows.

(1) There is little evidence of pulse-by-pulse driving of the Pi2 pulsation by the flow oscillation.
(2) The pulsation consisted of two frequencies, 10 and 19 mHz, with a weak third at 29 mHz.
(3) At RBSP-B and THEMIS-E, the 10-mHz oscillation was detected only in the azimuthal component of the electric field, while the 19-mHz oscillation was detected only in the compressional component of the magnetic field.
(4) On the ground, stations located at $L < 5$ detected both frequencies.
(5) The L profile of the phase of the ground Pi2 agrees with the result of the numerical simulation.
(6) Dayside Pi2 pulsation detected on the ground is not the result of direct propagation of the PVR mode to the dayside.

Acknowledgments
K. T. was supported by NASA grants NNX15AI95G and NNX17AD34G. M. D. H. was supported by NASA grant NNX17AD35G. R. L. L. was supported NSF grant AGS-1558134. The International Space Science Institute, Bern, facilitated collaboration of K. T., M. V., B. H., R. L., and D. H. L. Data used in this study are available from the following sources: Van Allen Probes Science Operation Centers located at University of Iowa (http://emfisis.physics.uiowa.edu) and University of Minnesota (http://www.space.umn.edu/missions/rbspefw-home-university-of-minnesota), for RBSP; Space Science Laboratory, University of California, Berkeley (http://themis.ssl.berkeley.edu), for THEMIS; NOAA National Centers for Environmental Information (http://satdat.ngdc.noaa.gov), for GOES; Japan Aerospace Exploration Agency (https://darts.isas.jaxa.jp/stp/geotail/data.html), for Geotail; Mining and Geological Survey of Hungary (http://geofizika.canet.hu/plasmon/, contact heilig.balazs@mbfsz.gov.hu), for EMMA; Kakioka Magnetic Observatory (http://www.kakioka-jma.go.jp/en/), for the Kakioka magnetometer; World Data Center for Geomagnetism, Kyoto (http://wdc.kugi.kyoto-u.ac.jp), for the *AL* and *AU* indices; and the United States Geological Survey (https://geomag.usgs.gov/monitoring/observatories/), for the San Juan and Honolulu magnetometers. The source data used for illustrating the results of the numerical simulation are available by contacting K. T. (kazue.takahashi@jhuapl.edu).

References

Allan, W., Menk, F. W., Fraser, B. J., Li, Y., & White, S. P. (1996). Are low-latitude Pi2 pulsations cavity/waveguide modes *Geophysical Research Letters*, *23*(7), 765–768. https://doi.org/10.1029/96gl00661

Angelopoulos, V., Kennel, C. F., Coroniti, F. V., Pellat, R., Kivelson, M. G., Walker, R. J., et al. (1994). Statistical characteristics of bursty bulk flow events. *Journal of Geophysical Research*, *99*(A11), 21,257–21,280. https://doi.org/10.1029/94ja01263

Auster, H. U., Glassmeier, K. H., Magnes, W., Aydogar, O., Baumjohann, W., Constantinescu, D., et al. (2008). The THEMIS fluxgate magnetometer. *Space Science Reviews*, *141*(1–4), 235–264. https://doi.org/10.1007/s11214-008-9365-9

Bendat, J. S., & Piersol, A. G. (1971). *Random data: Analysis and measurement procedures*. New York: John Wiley.

Bonnell, J. W., Mozer, F. S., Delory, G. T., Hull, A. J., Ergun, R. E., Cully, C. M., et al. (2008). The electric field instrument (EFI) for THEMIS. *Space Science Reviews*, *141*(1–4), 303–341. https://doi.org/10.1007/s11214-008-9469-2

Chen, L., & Hasegawa, A (1974). A theory of long-period magnetic pulsations: 1. Steady state excitation of field line resonance. *Journal of Geophysical Research*, *79*(7), 1024–1032. https://doi.org/10.1029/JA079i007p01024

Cummings, W. D., O'Sullivan, R. J., & Coleman, P. J. (1969). Standing Alfvén waves in the magnetosphere. *Journal of Geophysical Research*, *74*(3), 778–793. https://doi.org/10.1029/JA074i003p00778

Fairfield, D. H. (1969). Bow shock associated waves observed in the far upstream interplanetary medium. *Journal of Geophysical Research*, *74*(14), 3541–3553. https://doi.org/10.1029/JA074i014p03541

Fraser, B. J., Horwitz, J. L., Slavin, J. A., Dent, Z. C., & Mann, I. R. (2005). Heavy ion mass loading of the geomagnetic field near the plasmapause and ULF wave implications. *Geophysical Research Letters*, *32*, L04102. https://doi.org/10.1029/2004gl021315

Ghamry, E., Kim, K. H., Kwon, H. J., Lee, D. H., Park, J. S., Choi, J., et al. (2015). Simultaneous Pi2 observations by the Van Allen Probes inside and outside the plasmasphere. *Journal of Geophysical Research: Space Physics*, *120*, 4567–4575. https://doi.org/10.1002/2015ja021095

Green, C. A. (1976). The longitudinal phase variation of mid-latitude Pc3–4 micropulsations. *Planetary and Space Science*, *24*(1), 79–85. https://doi.org/10.1016/0032-0633(76)90064-7

Hsu, T.-S., McPherron, R. L., Angelopoulos, V., Ge, Y., Zhang, H., Russell, C., et al. (2012). A statistical analysis of the association between fast plasma flows and Pi2 pulsations. *Journal of Geophysical Research*, *117*, A11221. https://doi.org/10.1029/2012ja018173

Imajo, S., Yoshikawa, A., Uozumi, T., Ohtani, S., Nakamizo, A., & Chi, P. J. (2017). Application of a global magnetospheric-ionospheric current model for dayside and terminator Pi2 pulsations. *Journal of Geophysical Research: Space Physics*, *122*, 8589–8603. https://doi.org/10.1002/2017ja024246

Keiling, A., Kim, K. H., Wygant, J. R., Cattell, C., Russell, C. T., & Kletzing, C. A. (2003). Electrodynamics of a substorm-related field line resonance observed by the Polar satellite in comparison with ground Pi2 pulsations. *Journal of Geophysical Research*, *108*(A7), 1275. https://doi.org/1029/2002JA009340

Keiling, A., & Takahashi, K. (2011). Review of Pi2 models. *Space Science Reviews*, *161*(1–4), 63–148. https://doi.org/10.1007/s11214-011-9818-4

Kepko, L., & Kivelson, M. (1999). Generation of Pi2 pulsations by bursty bulk flows. *Journal of Geophysical Research*, *104*(A11), 25021–25034. https://doi.org/10.1029/1999ja900361

Kepko, L., Kivelson, M. G., & Yumoto, K. (2001). Flow bursts, braking, and Pi2 pulsations. *Journal of Geophysical Research*, *106*(A2), 1903–1915. https://doi.org/10.1029/2000ja000158

Kim, K. H., Takahashi, K., Ohtani, S., & Sung, S. K. (2007). Statistical analysis of the relationship between earthward flow bursts in the magnetotail and low-latitude Pi2 pulsations. *Journal of Geophysical Research*, *112*, A10. https://doi.org/10.1029/2007ja012521

Kim, K. H., Takahashi, K., Ohtani, S., Yumoto, K., Lee, D. H., Jin, H., et al. (2010). Substorm and pseudo-substorm Pi2 pulsations observed during the interval of quasi-periodic magnetotail flow bursts: A case study. *Earth, Planets and Space*, *62*(4), 413–425. https://doi.org/10.5047/eps.2009.12.003

Kivelson, M. G., & Southwood, D. J. (1986). Coupling of global magnetospheric MHD eigenmodes to field line resonances. *Journal of Geophysical Research*, *91*(A4), 4345–4351. https://doi.org/10.1029/JA091iA04p04345

Kletzing, C. A., Kurth, W. S., Acuna, M., MacDowall, R. J., Torbert, R. B., Averkamp, T., et al. (2013). The Electric and Magnetic Field Instrument Suite and Integrated Science (EMFISIS) on RBSP. *Space Science Reviews*, *179*(1–4), 127–181. https://doi.org/10.1007/s11214-013-9993-6

Kokubun, S., Yamamoto, T., Acuna, M. H., Hayashi, K., Shiokawa, K., & Kawano, H. (1994). The Geotail magnetic-field experiment. *Journal of Geomagnetism and Geoelectricity*, *46*(1), 7–21. https://doi.org/10.5636/jgg.46.7

Kurth, W. S., De Pascuale, S., Faden, J. B., Kletzing, C. A., Hospodarsky, G. B., Thaller, S., & Wygant, J. R. (2015). Electron densities inferred from plasma wave spectra obtained by the Waves instrument on Van Allen Probes. *Journal of Geophysical Research: Space Physics*, *120*, 904–914. https://doi.org/10.1002/2014JA020857

Kwon, H. J., Kim, K. H., Jun, C. W., Takahashi, K., Lee, D. H., Lee, E., et al. (2013). Low-latitude Pi2 pulsations during intervals of quiet geomagnetic conditions (Kp≤1). *Journal of Geophysical Research: Space Physics*, *118*, 6145–6153. https://doi.org/10.1002/jgra.50582

Lee, D.-H. (1998). On the generation mechanism of Pi2 pulsations in the magnetosphere. *Geophysical Research Letters*, *25*(5), 583–586. https://doi.org/10.1029/98gl50239

Lee, D. H., & Lysak, R. L. (1999). MHD waves in a three-dimensional dipolar magnetic field: A search for Pi2 pulsations. *Journal of Geophysical Research*, *104*(A12), 28691–28699. https://doi.org/10.1029/1999ja900377

Li, Y., Fraser, B. J., Menk, F. W., Webster, D. J., & Yumoto, K. (1998). Properties and sources of low and very low latitude Pi2 pulsations. *Journal of Geophysical Research*, *103*(A2), 2343–2358. https://doi.org/10.1029/97ja02921

Lichtenberger, J., Clilverd, M. A., Heilig, B., Vellante, M., Manninen, J., Rodger, C. J., et al. (2013). The plasmasphere during a space weather event: First results from the PLASMON project. *Journal of Space Weather and Space Climate*, *3*, A23. https://doi.org/10.1051/swsc/2013045

Liu, J., Angelopoulos, V., Zhang, X. J., Runov, A., Artemyev, A., Plaschke, F., et al. (2017). Ultralow frequency waves deep inside the inner magnetosphere driven by dipolarizing flux bundles. *Journal of Geophysical Research: Space Physics*, *122*, 10112–10128. https://doi.org/10.1002/2017ja024270

Love, J. J., & Finn, C. A. (2011). The USGS Geomagnetism program and its role in space weather monitoring. *Space Weather*, *9*, S07001. https://doi.org/10.1029/2011sw000684

Luo, H., Chen, G., & Du, A. (2014). Multipoint observations of Pi2 pulsations and correlation with dynamic processes in the near-Earth magnetotail on March 18, 2009. *Science China Earth Sciences*, *57*(2), 359–371. https://doi.org/10.1007/s11430-013-4632-3

Luo, H., Chen, G. X., Du, A. M., Angelopoulos, V., Xu, W. Y., Zhao, X. D., & Wang, Y. (2011). THEMIS multipoint observations of Pi2 pulsations inside and outside the plasmasphere. *Journal of Geophysical Research*, *116*, A12206. https://doi.org/10.1029/2011ja016746

Lyons, L. R., Nagai, T., Blanchard, G. T., Samson, J. C., Yamamoto, T., Mukai, T., et al. (1999). Journal of Geophysical Research, *104*(A3), 4485–4500. https://doi.org/10.1029/1998ja900140

McFadden, J. P., Carlson, C. W., Larson, D., Bonnell, J., Mozer, F., Angelopoulos, V., et al. (2008). THEMIS ESA first science results and performance issues. *Space Science Reviews*, *141*(1–4), 477–508. https://doi.org/10.1007/s11214-008-9433-1

Nishida, A. (1978). *Geomagnetic diagnosis of the magnetosphere*, vol. 9. New York: Springer-Verlag.
Nishimura, Y., Lyons, L. R., Kikuchi, T., Angelopoulos, V., Donovan, E., Mende, S., et al. (2012). Formation of substorm Pi2: A coherent response to auroral streamers and currents. *Journal of Geophysical Research*, *117*, A09218. https://doi.org/10.1029/2012ja017889
Nosé, M., Liou, K., & Sutcliffe, P. R. (2006). Longitudinal dependence of characteristics of low-latitude Pi2 pulsations observed at Kakioka and Hermanus. *Earth, Planets Space*, *58*, 775–783. https://doi.org/10.1186/BF03351981
Nosé, M., Oimatsu, S., Keika, K., Kletzing, C. A., Kurth, W. S., de Pascuale, S., et al. (2015). Formation of the oxygen torus in the inner magnetosphere: Van Allen Probes observations. *Journal of Geophysical Research: Space Physics*, *120*, 1182–1196. https://doi.org/10.1002/2014ja020593
Ohtani, S., Shay, M. A., & Mukai, T. (2004). Temporal structure of the fast convective flow in the plasma sheet: Comparison between observations and two-fluid simulations. *Journal of Geophysical Research*, *109*, A03210. https://doi.org/10.1029/2003ja010002
Olson, J. V., & Rostoker, G. (1975). Pi 2 pulsations and the auroral electrojet. *Planetary and Space Science*, *23*(8), 1129–1139. https://doi.org/10.1016/0032-0633(75)90163-4
Panov, E. V., Baumjohann, W., Nakamura, R., Kubyshkina, M. V., Glassmeier, K. H., Angelopoulos, V., et al. (2014). Period and damping factor of Pi2 pulsations during oscillatory flow braking in the magnetotail. *Journal of Geophysical Research: Space Physics*, *119*, 4512–4520. https://doi.org/10.1002/2013ja019633
Rowland, D. E., & Wygant, J. R. (1998). Dependence of the large-scale, inner magnetospheric electric field on geomagnetic activity. *Journal of Geophysical Research*, *103*(A7), 14959–14964. https://doi.org/10.1029/97ja03524
Saito, T., & Matsushita, S. (1968). Solar cycle effects on geomagnetic Pi 2 pulsations. *Journal of Geophysical Research*, *73*(1), 267–286. https://doi.org/10.1029/JA073i001p00267
Saito, T., Sakurai, T., & Koyama, Y. (1976). Mechanism of association between Pi2 pulsation and magnetospheric substorm. *Journal of Atmospheric and Terrestrial Physics*, *38*(12), 1265–1277. https://doi.org/10.1016/0021-9169(76)90135-5
Samson, J. C. (1982). Pi 2 pulsations: High latitude results. *Planetary and Space Science*, *30*(12), 1239–1247. https://doi.org/10.1016/0032-0633(82)90097-6
Shi, X., Baker, J. B. H., Ruohoniemi, J. M., Hartinger, M. D., Frissell, N. A., & Liu, J. (2017). Simultaneous space and ground-based observations of a plasmaspheric virtual resonance. *Journal of Geophysical Research: Space Physics*, *122*, 4190–4209. https://doi.org/10.1002/2016ja023583
Shiokawa, K., Baumjohann, W., Haerendel, G., Paschmann, G., Fennell, J. F., Friis-Christensen, E., et al. (1998). High-speed ion flow, substorm current wedge, and multiple Pi 2 pulsations. *Journal of Geophysical Research*, *103*(A3), 4491–4507. https://doi.org/10.1029/97ja01680
Singer, H. J., Matheson, L., Grubb, R., Newman, A., & Bouwer, S. D. (1996). Monitoring space weather with the GOES magnetometers. *Proceedings of the International Society for Optics and Photonics (SPIE)*, *2812*, 299–308. https://doi.org/10.1117/12.254077
Southwood, D. J. (1974). Some features of field line resonances in the magnetosphere. *Planetary and Space Science*, *22*(3), 483–491. https://doi.org/10.1016/0032-0633(74)90078-6
Sugiura, M., & Wilson, C. R. (1964). Oscillation of the geomagnetic field lines and associated magnetic perturbations at conjugate points. *Journal of Geophysical Research*, *69*(7), 1211–1216. https://doi.org/10.1029/JZ069i007p01211
Sutcliffe, P. R., & Lühr, H. (2010). A search for dayside geomagnetic Pi2 pulsations in the CHAMP low-Earth-orbit data. *Journal of Geophysical Research*, *115*, A05205. https://doi.org/10.1029/2009ja014757
Sutcliffe, P. R., & Yumoto, K. (1989). Dayside Pi 2 pulsations at low latitudes. *Geophysical Research Letters*, *16*(8), 887–890. https://doi.org/10.1029/GL016i008p00887
Takahashi, K., Anderson, R. R., & Hughes, W. J. (2003). Pi2 pulsations with second harmonic: CRRES observations in the plasmasphere. *Journal of Geophysical Research*, *108*(A6), 1242. https://doi.org/10.1029/2003ja009847
Takahashi, K., Anderson, B. J., & Ohtani, S. (1996). Multisatellite study of nightside transient toroidal waves. *Journal of Geophysical Research*, *101*(A11), 24815–24825. https://doi.org/10.1029/96ja02045
Takahashi, K., Lee, D. H., Nosé, M., Anderson, R. R., & Hughes, W. J. (2003). CRRES electric field study of the radial mode structure of Pi2 pulsations. *Journal of Geophysical Research*, *108*(A5), 1210. https://doi.org/10.1029/2002ja009761
Takahashi, K., Lysak, R., Vellante, M., Kletzing, C. A., Hartinger, M. D., & Smith, C. W. (2018). Observation and numerical simulation of cavity mode oscillations excited by an interplanetary shock. *Journal of Geophysical Research: Space Physics*, *123*, 1969–1988. https://doi.org/10.1002/2017ja024639
Takahashi, K., Ohtani, S.-I., & Anderson, B. J. (1995). Statistical analysis of Pi 2 pulsations observed by the AMPTE CCE spacecraft in the inner magnetosphere. *Journal of Geophysical Research*, *100*(A11), 21929–21941. https://doi.org/10.1029/95ja01849
Takahashi, K., Ohtani, S.-i., Hughes, W. J., & Anderson, R. R. (2001). CRRES observation of Pi2 pulsations: Wave mode inside and outside the plasmasphere. *Journal of Geophysical Research*, *106*(A8), 15,567–15,581. https://doi.org/10.1029/2001ja000017
Takahashi, K., Ohtani, S.-i., & Yumoto, K. (1992). AMPTE CCE observations of Pi 2 pulsations in the inner magnetosphere. *Geophysical Research Letters*, *19*(14), 1447–450. https://doi.org/10.1029/92gl0128
Teramoto, M., Takahashi, K., Nosé, M., Lee, D. H., & Sutcliffe, P. R. (2011). Pi2 pulsations in the inner magnetosphere simultaneously observed by the Active Magnetospheric Particle Tracer Explorers/Charge Composition Explorer and Dynamics Explorer 1 satellites. *Journal of Geophysical Research*, *116*, A07225. https://doi.org/10.1029/2010ja016199
Tsunomura, S., Yamazaki, A., Tokumoto, T., & Yamada, Y. (1994). The new system of Kakioka automatic standard magnetometer. *Memoirs of the Kakioka Magnetic Observatory*, *25*(1–2), 3–32.
Tsyganenko, N. A. (1989). A magnetospheric magnetic field model with a warped tail current sheet. *Planetary and Space Science*, *37*(1), 5–20. https://doi.org/10.1016/0032-0633(89)90066-4
Wu, Q., Du, A. M., Volwerk, M., Tsurutani, B. T., & Ge, Y. S. (2017). The distribution of oscillation frequency of magnetic field and plasma parameters in BBFs: THEMIS statistics. *Journal of Geophysical Research: Space Physics*, *122*, 4325–4334. https://doi.org/10.1002/2016ja023089
Wygant, J. R., Bonnell, J. W., Goetz, K., Ergun, R. E., Mozer, F. S., Bale, S., et al. (2013). The Electric Field and Waves instruments on the Radiation Belt Storm Probes Mission. *Space Science Reviews*, *179*(1–4), 183–220. https://doi.org/10.1007/s11214-013-0013-7
Yamaguchi, R., Kawano, H., Ohtani, S., Yumoto, K., Mukai, T., Saito, Y, & Hayakawa, H. (2002). The timing relationship between bursty bulk flows and Pi2s at the geosynchronous orbit. *Geophysical Research Letters*, *29*(6), 1092. https://doi.org/10.1029/2001GL013783
Yeoman, T. K., & Orr, D. (1989). Phase and spectral power of mid-latitude Pi2 pulsations: Evidence for a plasmaspheric cavity resonance. *Planetary and Space Science*, *37*(11), 1367–1383. https://doi.org/10.1016/0032-0633(89)90107-4
Yumoto, K., Osaki, H., Fukao, K., Shiokawa, K., Tanaka, Y., Solovyev, S. I., et al. (1994). Correlation of high- and low-latitude Pi 2 magnetic pulsations observed at 210° magnetic meridian chain stations. *Journal of Geomagnetism and Geoelectricity*, *46*(11), 925–935. https://doi.org/10.5636/jgg.46.925
Yumoto, K., Saito, T., Akasofu, S.-I., Tsurutani, B. T., & Smith, E. J. (1985). Propagation mechanism of daytime Pc3–4 pulsations observed at synchronous orbit and multiple ground-based stations. *Journal of Geophysical Research*, *90*(A7), 6439–6450. https://doi.org/10.1029/JA090iA07p06439